

X-ray spectral variations of Circinus X-1 observed with *NICER* throughout an entire orbital cycle

MAYU TOMINAGA ^{1,2} MASAHIRO TSUJIMOTO ¹ KEN EBISAWA ^{1,2} TERUAKI ENOTO ³ AND
KIMITAKE HAYASAKI ^{4,5}

¹*Institute of Space and Astronautical Science, Japan Aerospace Exploration Agency,
3-1-1 Yoshinodai, Chuo-ku, Sagami-hara, Kanagawa 252-5210, Japan*

²*Department of Astronomy, Graduate School of Science, The University of Tokyo,
7-3-1 Hongo, Bunkyo-ku, Tokyo 113-0033, Japan*

³*Division of Physics and Astronomy, Graduate School of Science, Kyoto University,
Kitashirakawa, Sakyo-ku, Kyoto 606-8502, Japan*

⁴*Department of Space Science and Astronomy, Chungbuk National University, Cheongju 361-763, Korea*

⁵*Harvard-Smithsonian Center for Astrophysics, 60 Garden Street, Cambridge, MA02138, USA*

(Received 18 Jul 2023; Accepted 03 Oct 2023)

ABSTRACT

Circinus X-1 (Cir X-1) is a neutron star binary with an elliptical orbit of 16.6 days. The source is unique for its extreme youth, providing a key to understanding early binary evolution. However, its X-ray variability is too complex to reach a clear interpretation. We conducted the first high cadence (every 4 hours on average) observations covering one entire orbit using the *NICER* X-ray telescope. The X-ray flux behavior can be divided into stable, dip, and flaring phases. The X-ray spectra in all phases can be described by a common model consisting of a partially covered disk black body emission and the line features from a highly-ionized photo-ionized plasma. The spectral change over the orbit is attributable to rapid changes of the partial covering medium in the line-of-sight and gradual changes of the disk black body emission. Emission lines of the H-like and He-like Mg, Si, S, and Fe are detected, most prominently in the dip phase. The Fe emission lines change to absorption in the course of the transition from the dip phase to the flaring phase. The estimated ionization degree indicates no significant changes, suggesting that the photo-ionized plasma is stable over the orbit. We propose a simple model in which the disk black body emission is partially blocked by such a local medium in the line-of-sight that has spatial structures depending on the azimuth of the accretion disk. Emission lines upon the continuum emission are from the photo-ionized plasma located outside of the blocking material.

Keywords: X-ray sources (1822), Atomic spectroscopy (2099), Spectroscopy (1558), Ionization (2068), Plasma astrophysics (1261), High energy astrophysics (739)

1. INTRODUCTION

Circinus X-1 (Cir X-1) is an X-ray binary system containing a neutron star (Margon et al. 1971) and a companion of an unidentified nature (Jonker et al. 2007; Johnston et al. 2001). It is unique for its extreme youth among all the known X-ray binaries; its association with the remnant of the supernova that produced the neutron star puts it at an estimated age of <4600 yr (Heinz et al. 2013). It is also the first X-ray binary from which the P Cygni profiles are clearly observed in the X-ray spectra (Brandt & Schulz 2000; Schulz & Brandt 2002), indicating the presence of disk winds around the neutron star. Such disk winds can contribute to the dissipation of the mass and angular momentum of the system, thereby influencing the evolution of the binary system (Begelman et al. 1983).

Despite the importance of Cir X-1 in many astrophysical contexts, the understanding of the system has been hampered by the notoriously wild behavior of the X-ray flux across various time scales. It has an orbital period of 16.6 days (Kaluzienski et al. 1976; Jonker et al. 2007) and a significant eccentricity of ~ 0.45 (Jonker et al. 2007). Across time scales longer than the orbital period, it shows drastic flux changes over a few orders of magnitude from a milli-Crab to a super-Crab. In time scales shorter than the orbital period, the X-ray flux changes as a function of the orbital phase in a regular (Kaluzienski et al. 1976) or an irregular (Asai et al. 2014) fashion. On the shortest time scales, it exhibits the twin kHz quasi-periodic oscillations (Tennant 1987) and type I bursts (Tennant et al. 1986; Linares et al. 2010), both of which are signatures of the accreting neutron stars with a low

magnetic field (van der Klis 2006). Among these variations across different time scales, the X-ray flux/spectral variations throughout the orbital phases are most critical for understanding the accretion disk states around the compact object.

Many studies have been made on the X-ray spectral components and their changes over the orbital period (e.g., Shirey et al. 1996; Brandt et al. 1996; Iaria et al. 2001, 2002; Schulz & Brandt 2002; Ding et al. 2006a,b; D’Ai et al. 2007; Schulz et al. 2008; Ding et al. 2012; Schulz et al. 2020). An important work among them is the detection of the emission and absorption lines of highly ionized metals in the high energy transmission grating (HETG) spectra with the *Chandra* X-ray Observatory, and a successful application of the photo-ionized plasma model in a low flux state (Schulz et al. 2008, 2020). Because *Chandra* observations are costly to cover the entire orbital cycle, the high-resolution spectra were obtained only at limited orbital phases including the periastron and apastron. An obvious next step is to cover the entire orbital phase with a spectral resolution capable of detecting the photo-ionized plasma emission and absorption features and constructing a model of the X-ray emitting objects. This is the goal of this paper using the new data set obtained with the Neutron Star Interior Composition Explorer (*NICER*; Gendreau et al. 2012, 2016) telescope covering an entire orbital period with a high cadence.

We start with the observation and data reduction in § 2 and present the X-ray light curve and spectral analysis in § 3. We then discuss an interpretation of the observed results with a simple model in § 4 and summarize the study

in § 5. Throughout the paper, we adopt the following; the distance to Cir X-1 of 9.4 kpc (Heinz et al. 2015), and the ephemerises of the periastron (Nicolson 2007) given by

$$t(N) = \text{MJD } 43076.32 + (16.57794 - 0.0000401 \times N) \times N \quad (1)$$

in which N is the cycle number since MJD 43076.32.

2. OBSERVATIONS AND DATA REDUCTION

NICER is an experiment located on the International Space Station (ISS) in near-Earth orbit at an altitude of ~ 400 km. The X-ray Timing Instrument (XTI) onboard *NICER* consists of 56 sets of the X-Ray Concentrator optics (XRC; Okajima et al. 2016) and the Silicon Drift Detector (SDD; Prigozhin et al. 2012). It has the capability of fast pointing with a robotic mechanism. XTI’s large effective area (600 cm² at 6 keV), moderate energy resolution (an FWHM of 137 eV at 6 keV), fast absolute timing precision (< 300 ns), and operational agility and flexibility opened an unexplored field for the timely X-ray spectroscopy of variable sources, uncompromised by photon statistics and dynamic range. These features are particularly suited for X-ray binaries, in which fast variability of up to a few kHz and orbital flux changes are commonly observed.

NICER usually conducts observations consisting of a short (≈ 500 s) snapshot with many targets in one ISS orbit of 90 minutes. Cir X-1 was observed with 103 snapshots totaling 61 ks (ObsID = 357801XX01, where XX=02 to 17 and 3578011502, which we hereafter identify with a sequential number from 0 to 102) over an orbital period with $\phi = 0.54\text{--}1.48$ from 2020-08-01 to 2020-08-16 (MJD=59062–59078). The average revisit time is ~ 3.9 hours, which corresponds to $\sim 1\%$ of the 16.6 day orbit.

We retrieved the level 2 products from the archive and processed them into the level 3

products using the `nicerl3` tools in `HEASOFT` version 6.31.1 and the calibration database version 20221001. The level 3 products include the X-ray light curves and spectra along with the redistribution matrix functions, the auxiliary response files, and background spectra, which we used for the timing and spectroscopy analysis. We modeled the background by SCORPEON model¹. The SCORPEON model produces a background model fitted along with the source spectrum including the following components; South Atlantic Anomaly (S), Cosmic Rays (COR), Polar and Precipitating Electrons (PE), constant terms (O), and Noise peak (N) of *NICER*.

3. ANALYSIS

We first explain the historical context of the *NICER* observation and present the X-ray light curve to define phases of the orbit based on flux changes (§ 3.1). We then select several representative spectra in each phase to construct spectral models and show that a common model can be applied to all phases despite apparent diversity (§ 3.2). Finally, we apply this common model to the entire data set and present the change in the spectral parameters across its orbit (§ 3.3) separately for the continuum (§ 3.3.1) and line (§ 3.3.2) components.

3.1. X-ray light curve

X-ray flux of Cir X-1 has been monitored for half a century. Light curves across three decades from 1968 to 2001 are given in (Parkinson et al. 2003), which we extended for two more decades up to 2023 in Figure 1. In the late 1990s and early 2000s, the observed flux exceeded a Crab, during which P Cygni profiles of highly-ionized metals were observed in X-ray grating spectra with *Chandra* (Brandt & Schulz 2000; Schulz & Brandt 2002). The flux declined to

¹ <https://heasarc.gsfc.nasa.gov/docs/nicer/analysis-threads/scorpeon-overview/>.

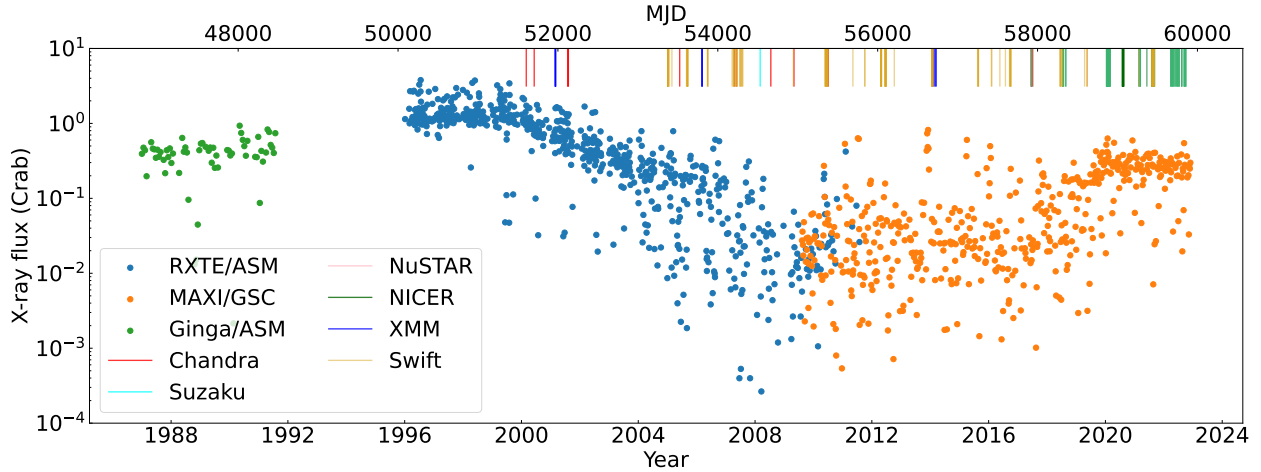


Figure 1. Long-term light curve of Cir X-1 observed with *Ginga*, *RXTE*, and *MAXI* all-sky monitors. Data points are sampled randomly for clarity. Vertical lines show the epochs of pointing observations with various X-ray telescopes.

the 10 mCrab level throughout the 2010s, during which emission-dominated spectra were observed (Schulz et al. 2020). From around 2018, the flux recovered to a few hundred mCrab at a similar level as in the 1980s. This is when repeated *NICER* observations were made in its AO1–4 cycles (green lines). We present the result of the data taken in the AO2 cycle in 2020.

After the flux recovered in 2018, the light curve folded by P_{orb} became more reproducible than that during the low-flux period, in which irregular flux changes specific to an orbit were often observed (Asai et al. 2014). Figure 2 shows the *NICER* light curve covering one orbit (top) compared to the *Monitor of All-sky X-ray Image* (*MAXI*) light curve (Matsuoka et al. 2009) of five preceding orbits (bottom). Before the periastron at $\phi = 1.0$, the flux drops by an order of magnitude for $\Delta\phi \sim 0.15$, which is often called “long dips” in the literature (e.g., Asai et al. 2014). After the periastron, the flux suddenly increases and becomes unstable for $\Delta\phi \sim 0.3$. The flux decreases gradually thereafter. The *NICER* data revealed these features at a higher significance and a finer time resolution than any previous data. The sharp ingress

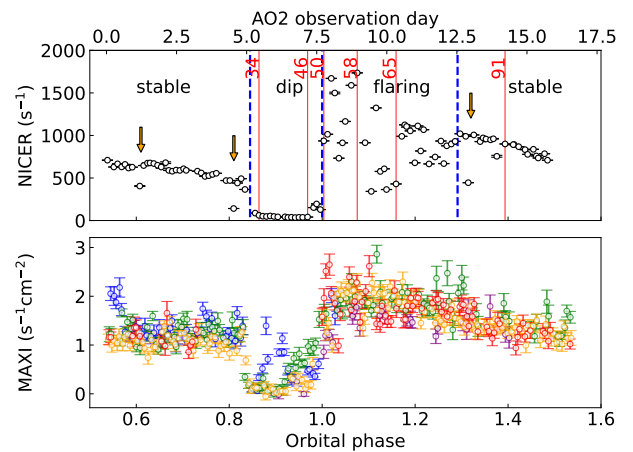


Figure 2. Light curves of the *NICER* AO2 observation covering the orbital phase of 0.54–1.48 (top) and the *MAXI* observation of the preceding five cycles of the same phase in different colors (bottom). In the top panel, the Bayesian-blocked phase boundaries are shown with blue dashed lines, while the data used for the spectral analysis representing each phase are shown with red solid lines with their snapshot numbers. Three orange arrows show the short dips.

and egress of the dips at $\phi = 0.83$ and 0.97 , the rapid fluctuations at $\phi = 1.0$ – 1.3 , and small dips at $\phi = 0.61$, 0.81 , and 1.32 (“short dips”) in a single orbit would not have been detected with-

out the *NICER*'s flexible and photon-rich observations.

We divide the *NICER* light curve into three phases using the Bayesian blocking method (Scargle et al. 2013). The boundaries are shown with the dotted horizontal lines in Figure 2. We label them the “dip” ($\phi \sim 0.84\text{--}1.0$), “flaring” ($\phi \sim 1.0\text{--}1.29$), and “stable” ($\phi \sim 0.54\text{--}0.84$ and $1.29\text{--}1.48$) phases. This division is consistent with the *ASCA* result (Iaria et al. 2001), in which three (dips, flaring, and stable) phases are recognized at $\phi = 0.78\text{--}0.97$, $0.93\text{--}0.3$, and $0.3\text{--}0.7$ based on observations covering one orbit in March 1998.

3.2. Modeling of X-ray spectra

We constructed the X-ray spectra in the 0.9—10.5 keV range for each of the 103 snapshots. This energy range was chosen to obtain a high signal-to-noise ratio. As for the representative spectra, we selected six spectra in the three phases and characterize them in § 3.2.1 (stable), § 3.2.2 (dip), and § 3.2.3 (flaring). For the spectral modeling, we included the attenuation by photo-electric absorption (Verner et al. 1996) from the interstellar medium (ISM) of the solar abundance (Wilms et al. 2000). The spectra were rebinned to have at least 30 counts per energy bin and ensure the use of χ^2 statistics.

3.2.1. Stable phase

We start with the stable phase. The continuum spectral shape shows only a gradual decrease in flux. This is shown in snapshot 91's data in Figure 3 (f). The continuum emission can be modeled with a simple disk black body component (Mitsuda et al. 1984; Makishima et al. 1986) with two fitting parameters (the normalization and the innermost disk temperature T_{in}), partially covered by a neutral cloud with two parameters (the covering fraction $f^{(\text{cov})}$ and the H-equivalent column density $N_{\text{H}}^{(\text{cov})}$) and interstellar absorption with a fixed column density of $2.0 \times 10^{22} \text{ cm}^{-2}$. Schulz et al.

(2008) showed that there can be several types of covering matter with different degrees of ionization along the line-of-sight. Our data did not allow us to distinguish these different types, thus we only assumed neutral matter. We further added the Gaussian model to account for the Fe K fluorescence line at 6.4 keV.

3.2.2. Dip phase

We next investigate the dip phase. The spectral shape changed in the middle of the dip phase. During the period of the first ten data points (hereafter “the early dip” period), the spectral shape exhibits one peak, which we represent with snapshot 34 (Fig. 3a). In contrast, during the period of the remaining six data points (hereafter “the late dip” period), the shape exhibits two peaks, which we represent with snapshot 46 (Fig. 3b). Despite the difference, both can be described with different parameters of the same model. The two peaks are, in fact, reproduced by uncovered and covered components of the partially covered disk black body emission. The spectra in this phase are also characterized by numerous emission lines, most notably in highly ionized Fe, but also in lighter metals such as Mg, Si, and S. We fit them with Gaussian lines likely originating from a photo-ionized plasma. The plasma emission should accompany continuum emission in the soft band. In fact, we did observe excess emission in the softest end of the spectrum, which we phenomenologically represented with a power-law model.

3.2.3. Flaring phase

There are significant flux variations in the flaring phase (Fig. 2). We chose three snapshots representing high, medium, and low flux (snapshot 58, 50, and 65), respectively). The flux varies by a factor of >5 , but the spectral shape does vary as much. We thus applied the same model (partially covered disk black body emission) and we were able to model the spectra

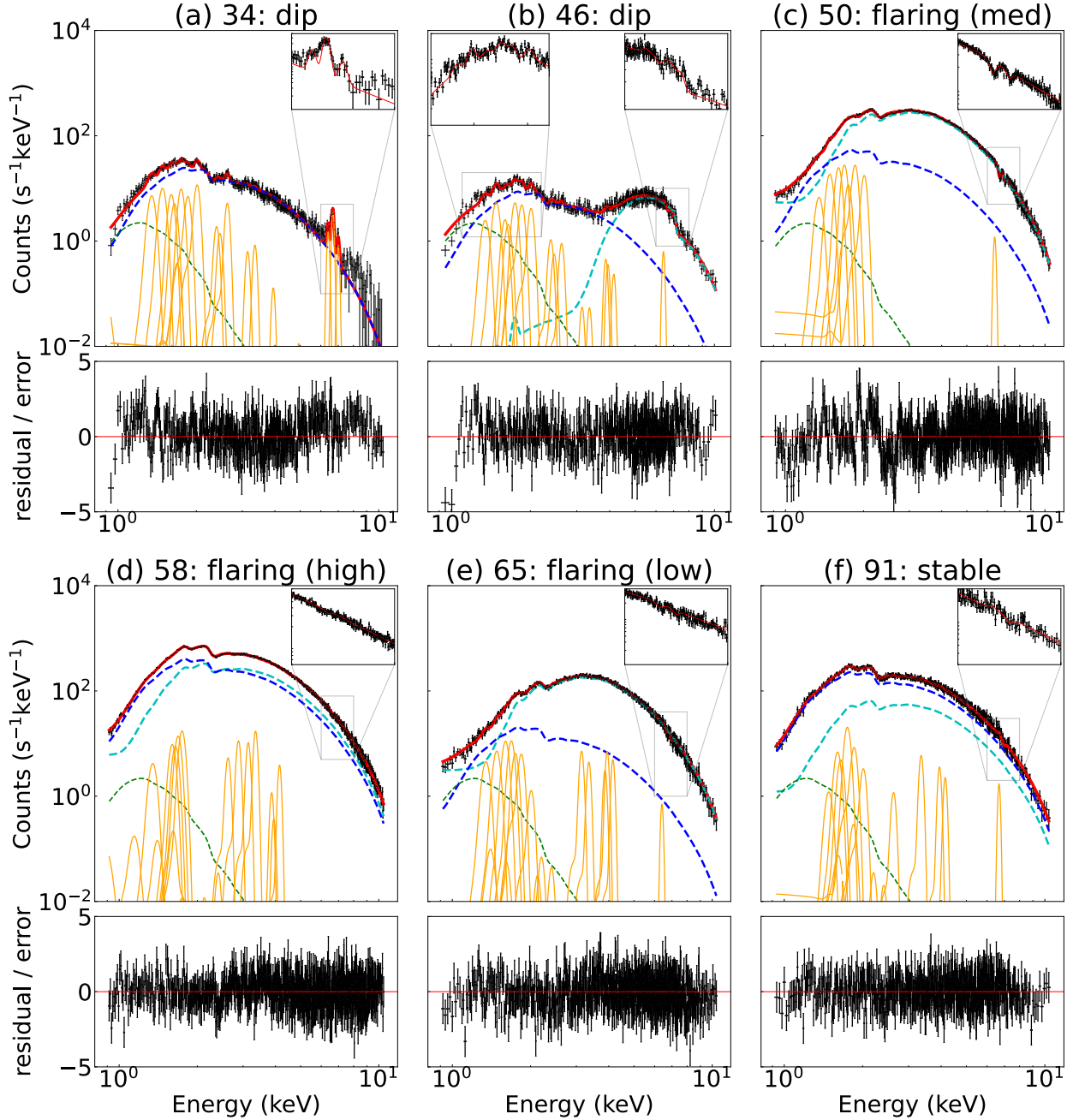


Figure 3. Spectra (black) and best-fit model in the top panels and the residuals to the fit in the bottom panels for the six snapshot spectra representing the dip (a and b), flaring (c, d, and e), and stable (f) phases. Different colors are used for different model components; red for total, cyan for covered disk black body, blue for uncovered disk black body, orange for Gaussian models, and green for soft excess. The insets give a close-up view of the energy bands with apparent spectral line features.

through variations in the covering fraction and column density of the partial covering component. Several Gaussian lines were added, both

positive and negative in flux, to account for the emission and absorption features, respectively.

3.2.4. All the phases

To summarize the result in § 3.2.1–§ 3.2.3, despite the variety of the spectral shapes, the spectra of the six selected snapshots were described well with the same approach; the disk black body emission partially covered by neutral cloud and fully covered by the ISM photoelectric absorption. Some minor differences remain, such as the soft excess emission required for the late dip phase (Fig. 3b) and the Gaussian lines observed either positive (emission) or negative (absorption) in different phases.

We thus constructed a common model to encompass these minor differences. The soft excess was required only in the dip phase, but we included this component in all phases with the parameters fixed to the parameter values derived from the dip phase. This does not influence the fitting in other phases, as the soft excess is overwhelmed by the uncovered disk black body emission. We also added Gaussian lines at the energies of $\text{Ly}\alpha$ and $\text{He}\alpha$ transitions of H-like and He-like ions of Mg, Si, S, and Fe plus Fe I $\text{K}\alpha$ fluorescence. Here, the $\text{He}\alpha$ line refers to all unresolved lines of $(1s)(2p)$ or $(1s)(2s) \rightarrow (1s)^2$ transitions, while the $\text{Ly}\alpha$ line refers to $(2p) \rightarrow (1s)$ transitions. We allowed both positive and negative values in the fit to account for both emission and absorption. No significant Doppler shift or broadening was observed in any of these lines, thus we fixed the line energy shift and width to 0. The best-fit models shown in Figure 3 are the results of applying this common model.

In the previous work of Cir X-1, the X-ray continuum spectra were often explained by a combination of multiple spectral components of a black body, disk black body, and Comptonized emission (e.g., Shirey et al. 1999; Iaria et al. 2005; D’Ài et al. 2012). We argue that a single disk black body component is sufficient to explain the variety of spectra for the present data set. The partial coverage of the disk black body emission alone can make two continuum

peaks for the covered and uncovered parts. The addition of a black body component was not required in all spectra throughout the orbit. We note that the actual emission would be a mixture of emissions from the neutron star surface, the boundary layer, and the accretion disk, but a single disk black body component is sufficient to explain the data.

3.3. Change of X-ray spectra

Having constructed a common spectral model using the six selected snapshots, we apply it uniformly to the spectra of all 103 snapshots. Although the fitting did not work for some individual spectra, the overall variation of the spectral parameters throughout the orbit could be characterized with this method. We first track the phase-dependent change of the parameters of the continuum components (§ 3.3.1) and then those of the line components (§ 3.3.2).

3.3.1. Continuum

The phase-dependent change of the spectral model parameters for the continuum components is given in green symbols in Figure 4. The free parameters are the normalization and T_{in} for the disk black body emission and $f^{(\text{cov})}$ and $N_{\text{H}}^{(\text{cov})}$ for the partial covering absorption. To mitigate a degeneracy in the parameters space, firstly we fitted the data only above 4 keV, obtained the best-fit T_{in} values. We then fitted using all the available energy range with the fixed T_{in} values.

In the stable phase, the parameters change gradually. Some spectra do not require the partial covering material, thus we fixed both $N_{\text{H}}^{(\text{cov})}$ and $f^{(\text{cov})}$ to null. In the flaring phase, we found that the fitting results widely vary, in particular, for normalization. As this parameter represents the entire disk luminosity, it is inconceivable that it changes as rapidly as the revisit time of ~ 4 hours. We thus constrained its variation with a low-pass-filtered trend as shown with red symbols in Figure 4. The rapid variation is now

attributed mostly to the changes in the partial coverage.

The trend of the normalization was further extrapolated backward to the late dip phase, which yielded acceptable fits. However, this did not work for the early dip phase. This is because of the different appearance of the spectral shape as exemplified in the spectra from snapshot 34 and 46 (Fig. 3). In the late dip, we observe both the partially covered and uncovered disk black body emission. In the early dip, we only observe the uncovered component, as the covered component is attenuated too much to be visible in the *NICER* energy band. The degeneracy between the following two cases cannot be broken in the fitting: (a) a large value of the partial covering column or (b) a small value of the disk normalization with a small covering column. The solution (b) yields fitted results with a large scatter in the disk black body parameters (T_{in} and normalization), which is unlikely. We thus opted for (a) by constraining the partial covering column to be $> 10^{24} \text{ cm}^{-2}$ for the best-fit parameter. For this reason we include large error estimates in the early dip phase in Figure 4. The *NICER* data do not allow us to track the trend of the disk black body parameters during the early dip phase.

3.3.2. Lines

The phase-dependent change of the line normalization parameter is given in Figure 5 separately for Mg, Si, S, and Fe. Different colors are used for the H-like and He-like ions.

For Mg, Si, and S, emission lines were detected in almost all the snapshots mainly during the dip phase. During the dip phase, their normalization decreases, particularly, in the late dip phase.

For Fe, a more stringent constraint was obtained, revealing changes between the emission and absorption features. In the dip phase, the line appears as emission at the beginning for the early dip, but the line normalization decreases

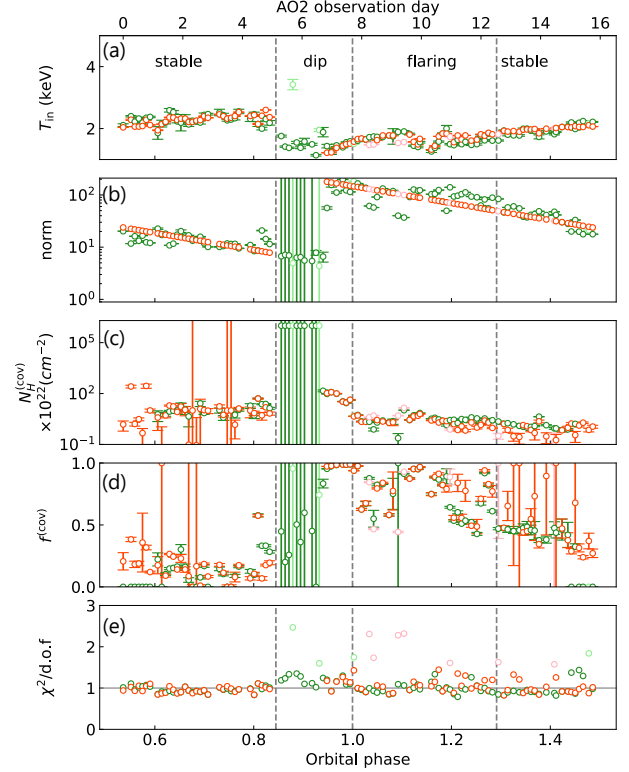


Figure 4. Phase-dependent change of the best-fit parameters for the continuum model: (a) T_{in} and (b) normalization of the disk black body emission, and (c) $N_{\text{H}}^{(\text{cov})}$ and (d) $f^{(\text{cov})}$ of the partial covering material. (e) The reduced χ^2 value of the fitting is also given. The green symbols represent the results without constraining the normalization parameter values, whereas the red symbols, except for the early dip period, are those with the normalization values constrained along the global trend. Pale colors are for those with unacceptable fitting with a reduced χ^2 greater than 1.5, which we ignore when investigating overall spectral change.

in the late dip similar to the other elements. In the end, the line feature changed from emission to absorption, which continues for the flaring phase and reverts back to emission in the stable phase.

4. DISCUSSION

Based on the characterization of the entire data set in § 3, we discuss the interpretation. We first present the assumed geometry (§ 4.1),

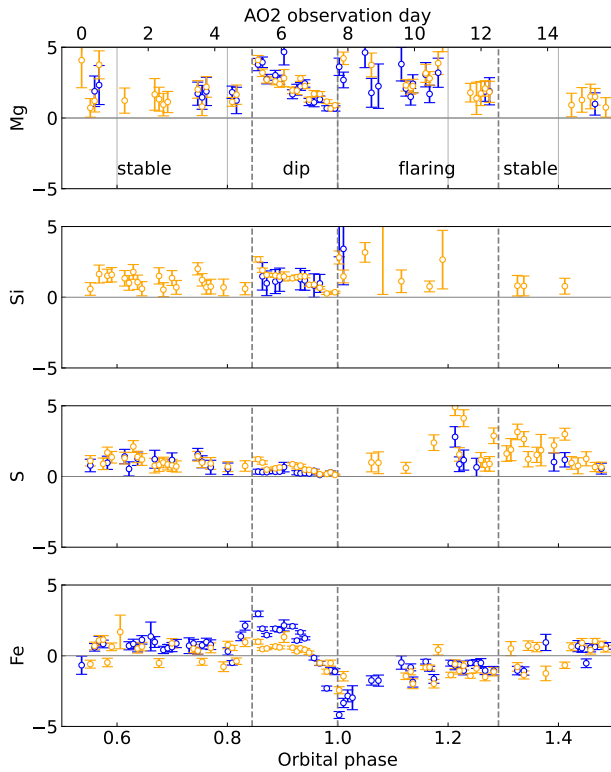


Figure 5. Normalization ($\times 10^{-3} \text{ s}^{-1} \text{ cm}^{-2}$) of the line (positive for emission and negative for absorption) for He-like (blue) and H-like (orange) ions using the $\text{He}\alpha$ and $\text{Ly}\alpha$ lines of Mg, Si, S, and Fe. We omit the snapshots either with the reduced χ^2 greater than 1.5 or the line normalization consistent with zero.

which we rationalize by using a suite of observed results (§ 4.2), then we make some quantitative assessment of the geometry (§ 4.3).

4.1. Proposed Model

Our assumed geometry is shown in Figure 6, in which the optically-thin plasma extends away from the accretion disk. This picture is different from the conventional interpretation of the “(hot) accretion disk corona”, in which an optically-thin plasma exists on the surface of the disk. The plasma is produced by being illuminated by the incident X-ray emission from the surface of the neutron star and the accretion disk around it. The plasma emits diffuse emission through radiative de-excitation and recom-

bination. The incident X-ray emission transmits through the plasma, in which absorption lines and edges are imprinted by radiative excitation and ionization. The balance between them depends on the ratio of the transmitted and diffuse emission determined by the geometry in the line-of-sight and the incident X-ray flux.

We assume that a geometrically-flared optically-thick medium exists locally in the outer part of the accretion disk. Such a structure is called the “bulge” in some literatures (e.g., White & Swank 1982). We speculate that this is the accretion spot of the material from the companion star, which is hinted at observationally (e.g., Groot et al. 2001; Hynes et al. 2001; Hellier 1996; Casares et al. 2003) and envisioned theoretically (Armitage & Livio 1998). We do not delve into the detailed interpretation of what the covering media are. All we need is a localized structure that can provide a complete or partial covering of the X-ray emission from the neutron star and accretion disk, in which the covering column and fraction change as the sight line changes along the binary orbit.

4.2. Rationale

We use four results to rationalize the proposed model. The first result is the presence of the disk black body emission throughout the orbital cycle. Its parameters change only gradually on the orbital time scale. The flux variations are much faster than the orbital period primarily due to covering by the medium outside the disk blackbody radiation region. (Fig. 4).

The second result is the presence of the dip and flaring phases. The local covering medium should have some density and clumpy structure depending on the disk’s azimuth, so that it creates changes in the line-of-sight as a function of the orbital phase. The X-ray flux dip starts when the densest part of the covering medium comes in the line-of-sight. The total covering column decreases, resulting in the spectral

changes between the early and the late halves of the dip phase (§ 3.2.2). This dense material is broken into pieces in the tail part, which creates the rapid flux variation during the flaring phase (§ 3.2.3).

The third result is the appearance of the Fe line feature either as emission or absorption in addition to the disk emission (§ 3.3.2). The feature is made by highly-ionized Fe in the photo-ionized plasma. When it appears as absorption, the incident disk emission transmitted through the photo-ionized plasma surpasses the diffuse emission from the plasma. When it appears as emission, the transmitted emission is insignificant by being blocked in the line-of-sight, and the diffuse emission from the plasma is dominant.

The fourth result is the stability of the emission line strength compared to the total flux. The total flux decreases by an order of magnitude in the dip phase (Fig. 2), while the emission lines do not (Fig. 5). This indicates that most of the photo-ionized plasma is not blocked by the local medium, unlike the disk black body emission.

When all these are combined, we came to a model depicted in Figure 6. The edge-on view for the early dip, late dip + flaring, and stable phases are shown in (a), (b), and (c), respectively.

4.3. Assessments

We make two quantitative assessments based on the geometry proposed in Figure 6. One is the ionization parameter of the photo-ionized plasma (§ 4.3.1) and the other is the system scale (§ 4.3.2).

4.3.1. Ionization parameter

We use the emission or absorption line features to derive ionization parameters. We calculate the intensity ratio between the Ly α and He α lines when both of them are detected. The emission line pair was detected for Mg in the dip

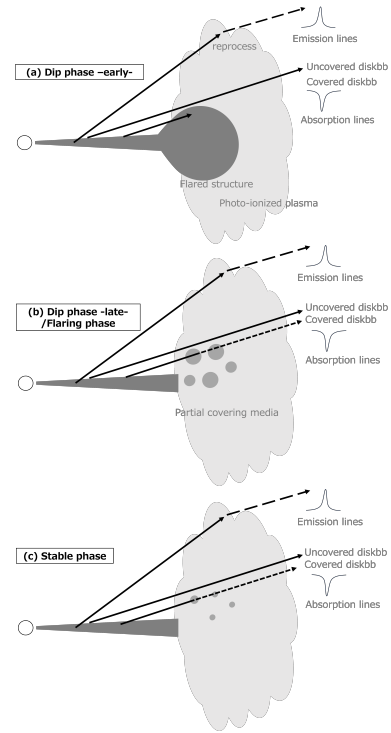


Figure 6. Proposed view of the system: edge-on views during the (a) dip (early), (b) dip (late)/flaring, and (c) stable phases, respectively. The local blocking medium has some spatial structures depending on the disk azimuth, making changes in the line of sight as a function of the orbital phase.

phase and for Fe throughout orbit, while the absorption line pair was detected for Fe from the end of the dip phase to the flaring phase.

We employ the `xstar` code (Kallman & Bautista 2001) to numerically estimate the expected line ratio of the pairs. The code solves the radiative transfer equation for the non-local thermal equilibrium condition for the charge and level populations in the photo-ionized plasma by balancing radiative cooling and heating, ionization and recombination, and excitation and de-excitation. It uses the two-stream approximation solver in the inward and outward directions. The energy input (incident emission) is given and the outputs (transmitted emission and diffuse emission inward and outward) are calculated.

Because the `xstar` code is only for one-dimensional geometry, we approximated the photo-ionized plasma as a plane-parallel slab. The slab is static, uniform, and optically thin for the electron scattering with hydrogen density of $n_{\text{H}} = 3 \times 10^{14} \text{ cm}^{-3}$ and column density of $N_{\text{H}} = 1 \times 10^{18} \text{ cm}^{-2}$. The incident emission has the shape of the disk black body with representative parameters over the stable phase.

For the emission lines, they are mainly produced as a result of the recombination cascades of e.g., Fe^{26+} and Fe^{25+} for Fe. The $\text{Ly}\alpha$ to $\text{He}\alpha$ ratio is thus very sensitive to the ionization parameter $\xi = L/(n_e r^2)$, in which n_e is the electron density and r is the distance from the incident source to the slab. We took into account the effect of radiative excitation by the incident emission, which is known to alter the line strength when a large fraction of the incident emission is outside of the beam (Kinkhabwala et al. 2002) as in the dip phase. The expected line ratio was calculated as a function of $\log \xi$ ($\text{erg s}^{-1} \text{ cm}$) over 0–5 in increments of 0.1 and a ξ value was selected that matches the observed ratio.

For the absorption lines, we followed the same procedure but evaluated the column density of Fe^{25+} and Fe^{24+} through the slab that is responsible for the absorption lines respectively of $\text{Ly}\alpha$ and $\text{He}\alpha$ by absorbing the incident emission at each transition energy. These column densities are related to the observed equivalent width through the curve of growth. We selected the best $\log \xi$ value to reproduce the observed ratio between the two lines.

The result is shown in Figure 7. The ξ values using the Mg, Si, S emission, Fe emission and Fe absorption pair are, respectively, $\sim 1.9 \pm 0.02$, $\sim 2.1 \pm 0.04$, $\sim 2.5 \pm 0.02$, $\sim 3.4 \pm 0.04$ and $\sim 3.7 \pm 0.08$ for the means and standard deviations. They differ to some extent, which indicates that the actual photo-ionized plasma has a stratified ionization structure of varying ξ as

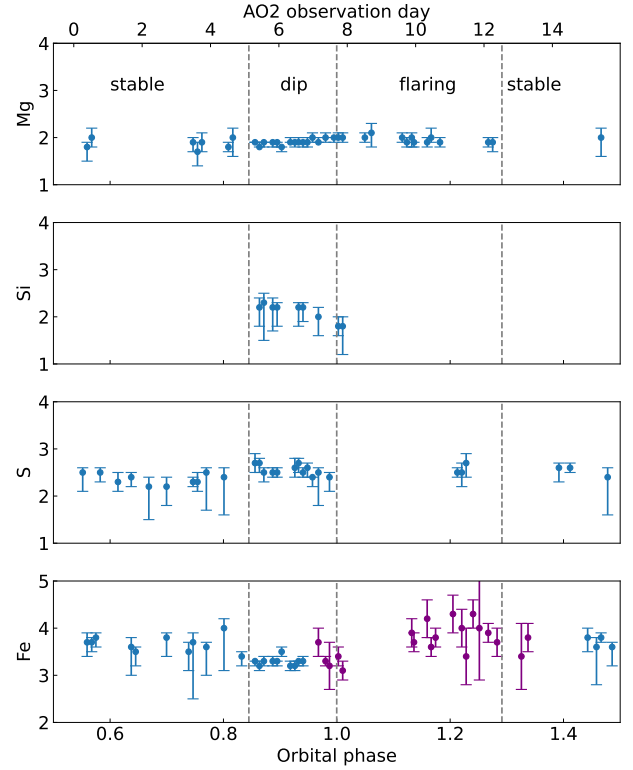


Figure 7. Best-fit ionization parameter (ξ) by comparing the observed and simulated line ratio of $\text{Ly}\alpha$ and $\text{He}\alpha$ lines for snapshots, in which both features are significantly detected. Blue symbols indicate values obtained using the emission line pairs and purple symbols indicate those using absorption line pairs.

suggested in Schulz et al. (2008). However, they are stable across different phases. This suggests that the photo-ionized plasma remains mostly unchanged throughout the orbital cycle. The ξ values using the Fe emission and absorption features match well, indicating that the differences are created by changes in the viewing geometry and/or the incident X-ray flux, not by changes in the photoionized plasma itself.

In the dip phase, it should be noted that the Fe line pairs changed from emission to absorption in the middle at $\phi = 0.95$ before this phase ends (Fig. 5). Since the emission from the photo-ionized plasma is considered stable over orbit, this change should be created by an in-

crease in the fraction of the incident emission through the photo-ionized plasma, which contributes to the absorption lines. This is presumably made by the increase of both the normalization of the disk black body emission and the decrease of the partial covering fraction in the line-of-sight as shown in Figure 4(d) and depicted in Figure 6.

4.3.2. System scale

The size of the system can be estimated by assuming the electron density n_e . The *NICER* data are incapable of constraining this value, so we used the estimate of the upper limit (10^{15} cm^{-3}) given by the *Chandra* grating spectroscopy of the triplet lines of He-like ions (Schulz et al. 2020).

We estimate the size of the photo-ionized plasma. The inner radius $r_{\text{in}} = \sqrt{L_X/(\xi n_e)} \sim 10^{10} \text{ cm}$ for the best-fit $\log \xi$ parameter for Fe emission and the observed disk luminosity of L_X . The r_{in} value is a lower limit as we used an upper limit for n_e .

The outer radius (r_{out}) is constrained by the observed the maximum total amount of Fe absorption column by

$$N_{\text{Fe}i+} \sim f_{\text{Fe}i+} A_{\text{Fe}} n_{\text{H}} (r_{\text{out}} - r_{\text{in}}), \quad (2)$$

in which $N_{\text{Fe}i+}$ is the observed absorption column of the Fe^{i+} ions ($i \in \{24, 25\}$), $f_{\text{Fe}i+}$ is the charge fraction of the ion among all Fe, A_{Fe} is the assumed solar Fe abundance relative to H, and n_{H} is the H density, which we approximate as $n_{\text{H}} = n_e$. The Fe column is derived from the observed equivalent width through the curve of growth. The charge fraction and the curve of growth are derived from an XSTAR simulation, in which the column density of the slab $\log N_{\text{H}} \text{ cm}^{-2}$ was changed 15–25 in increments of 1 for the ionization degree of $\log \xi = 3.5 \text{ erg s}^{-1} \text{ cm}$. We used snapshot 50 and 65 (Fig. 3 c and e, respectively) where the Fe absorption features were strong. For both H-like ($i = 25$) and He-like ($i = 24$) ions, the result

is in the range of $r_{\text{out}} - r_{\text{in}} = 10^{9-10} \text{ cm}$. The photo-ionized plasma has some structures for different ξ values for different elements (§ 3.3.2). The part contributing to the Fe features is relatively thin with $r_{\text{out}}/r_{\text{in}} = 1.1 - 2$.

This still yields strong emission lines from the plasma. XSTAR calculates that Fe XXV He α will be $6\text{--}120 \times 10^{36} \text{ erg s}^{-1}$ for $N_{\text{H}} = 10^{24-25} \text{ cm}^{-2}$, which is much larger than the observed value of $1.7 \times 10^{35} \text{ erg s}^{-1}$. This is the case in the dip phase when there is no significant absorption features imprinted in the disk black body emission that cancels the emission. Therefore, we consider that the volume filling factor of the photo-ionized plasma is small in comparison to the xstar assumption of a spherical medium.

We further compare the inner and outer radius of the photo-ionized plasma (r_{in} and r_{out}) with those of the accretion disk (R_{in} and R_{out}). In our spectral analysis, the normalization of the disk black body emission is related to R_{in} as $(R_{\text{in}}/0.94)^2 \cos \theta$, in which θ is the viewing angle. For a complete edge-on $\theta = 0$ and the normalization of 100 (the largest in the trend in Fig. 4b when a large fraction of the disk is considered to be exposed), we obtain $R_{\text{in}} \sim 10^6 \text{ cm}$. The R_{in} value is close to a typical value of a neutron star radius since the accretion disk is thought to stretch inward almost close to the neutron star surface (e.g., Frank et al. 2002).

We cannot constrain R_{out} from the present data. At least, it must be smaller than the effective Roche lobe radius of the binary of $\sim 10^{10} \text{ cm}$ (Begelman et al. 1983). If we assume that a typical value for low mass X-ray binaries of $R_{\text{out}} \sim 10^{9-10} \text{ cm}$ (Jimenez-Garate et al. 2002) is applicable to Cir X-1, $r_{\text{in}} \gtrsim R_{\text{out}}$, suggesting that the photo-ionized plasma is located outside of the accretion disk.

5. SUMMARY

We present the result of *NICER* observations covering an entire orbital period of Cir

X-1. Thanks to its operational flexibility and unprecedented large collecting area with moderate energy resolution, we obtained well-exposed spectra along the orbital phase with sufficient cadence, energy resolution, and uniform quality. Using this unique data set, we obtained the following results and implications.

1. The flux change over an orbit is repeated reproducibly by comparing to the *MAXI* light curves of preceding orbits. It is divided into three parts; dip, flaring, and stable phases.
2. We constructed spectral models for representative spectra in each phase. Despite the apparent changes, we argue that they can be described by a common model with different parameters.
3. The continuum emission is explained by a variable disk black body component over the entire orbit, with a minor invariable soft-excess component expected from the photo-ionized plasma.
4. The variety of the X-ray flux changes and the continuum spectral shape is mostly attributable to rapid changes of the partial covering material in the line-of-sight and gradual changes of the accretion disk temperature and luminosity.
 - (a) The dip phase, which occupies $\sim 15\%$ of the orbit before and at the periastron, is characterized by a sudden decrease in the X-ray flux. It is attributable to a sudden increase in the absorption column of the partial covering material in the line-of-sight provided that the disk black body emission gradually changes.
 - (b) The following flaring phase for $\sim 30\%$ of the orbit is characterized by rapid changes of the X-ray flux, which is mostly attributable to rapid changes of the covering fraction of the partially covering medium in the line-of-sight.
 - (c) The stable phase is characterized by a gradual decrease of the X-ray flux. This is governed by the gradual change of the disk black body emission.
5. Upon the continuum emission, we found emission and absorption features from the H-like and He-like ions of Mg, Si, S, and Fe. They are presumably from the extended photo-ionized plasma. They are most evident during the dip phase when the continuum emission of the disk black body is most attenuated. The Fe line feature turns from emission to absorption in the middle of the dip phase.
6. Using a pair of Ly α and He α lines respectively of H-like and He-like Mg, Si, S, and Fe, we derived the change of the ionization parameter as a function of the orbital phase. The ionization parameter value remains stable, regardless of whether the pair appears in emission or absorption, suggesting that the photo-ionized plasma remains almost unchanged over an orbit.
7. We proposed an interpretation to explain these findings. A photo-ionized plasma illuminated by the incident X-ray emission from the accretion disk and the neutron star is located radially outside of the accretion disk, not on its surface. The disk black body emission is blocked in the early dip phase due to a geometrically flared medium which is present only for a subtended small azimuth angle range of the accretion disk. The medium has some density and fragmentation structure, the variation of which generates the X-ray flux and spectral changes in the late dip and flaring phases.

8. We estimated the scales of these structures. The photo-ionized plasma responsible for the Fe line features is estimated to be located adjacently outside of the accretion disk.

The sampling frequency of the orbital spectral variation presented in this study is much denser than in the previous Cir X-1 studies. Yet, we presented a much simpler spectral model. We recognize that a few spectra yielded bad fitting, but they do not alter the overall interpretation presented here. A geometry was proposed to explain these findings. We argue that the proposal will help disentangle the complex behaviors of this source observed in other instruments at different flux ranges and energy ranges and guide toward a better understanding of the unique binary system.

Facility: NICER (Gendreau et al. 2012)

Software: HEASoft (Nasa High Energy Astrophysics Science Archive Research Center (Heasarc) 2014), Xspec (Arnaud 1996), XSTAR (Kallman et al. 2004)

1 We appreciate careful proofreading by Fred-
 2 erick T. Matsuda at ISAS/JAXA and Juriko
 3 Ebisawa. M.T. is financially supported by
 4 the JSPS grant number 21J20947. K.H. has
 5 been supported by the Basic Science Research
 6 Program through the National Research Foun-
 7 dation of Korea (NRF) funded by the Min-
 8 istry of Education (2016R1A5A1013277 and
 9 2020R1A2C1007219). This work was finan-
 10 cially supported by the Research Year of Chung-
 11 buk National University in 2021. This work
 12 made use of the JAXA's super-computing sys-
 13 tem JSS3. This research has made use of data
 14 and/or software provided by the High Energy
 15 Astrophysics Science Archive Research Center
 16 (HEASARC), which is a service of the As-
 17 trophysics Science Division at NASA/GSFC.
 18 This research also made use of data ob-
 19 tained from Data ARchives and Transmis-
 20 sion System (DARTS), provided by Center for
 21 Science-satellite Operation and Data Archive
 22 (C-SODA) at ISAS/JAXA, including the MAXI
 23 data provided by RIKEN, JAXA and the MAXI
 24 team.

REFERENCES

- Armitage, P. J., & Livio, M. 1998, *The Astronomical Journal*, 493, 898
- Arnaud, K. A. 1996, *Astronomical Data Analysis Software and Systems V*, A.S.P. Conference Series, 101, 17
- Asai, K., Mihara, T., Matsuoka, M., et al. 2014, *Publications of the Astronomical Society of Japan*, 66, 79, doi: [10.1093/pasj/psu054](https://doi.org/10.1093/pasj/psu054)
- Begelman, M. C., McKee, C. F., & Shields, G. A. 1983, *The Astrophysical Journal*, 271, 70, doi: [10.1086/161178](https://doi.org/10.1086/161178)
- Brandt, W. N., Fabian, A. C., Dotani, T., et al. 1996, *Monthly Notices of the Royal Astronomical Society*, 283, 1071, doi: [10.1093/mnras/283.3.1071](https://doi.org/10.1093/mnras/283.3.1071)
- Brandt, W. N., & Schulz, N. S. 2000, *The Astrophysical Journal*, 544, L123, doi: [10.1086/317313](https://doi.org/10.1086/317313)
- Casares, J., Steeghs, D., Hynes, R. I., Charles, P. A., & O'Brien, K. 2003, *The Astrophysical Journal*, 590, 1041, doi: [10.1086/375055](https://doi.org/10.1086/375055)
- D'Ai, A., Iaria, R., Di Salvo, T., et al. 2007, *The Astrophysical Journal*, 671, 2006, doi: [10.1086/522565](https://doi.org/10.1086/522565)
- D'Ai, A., Bozzo, E., Papitto, A., et al. 2012, *Astronomy & Astrophysics*, 543, A20, doi: [10.1051/0004-6361/201118577](https://doi.org/10.1051/0004-6361/201118577)
- Ding, G., Huang, C., & Qu, J. 2012, *International Journal of Astronomy and Astrophysics*, 02, 256, doi: [10.4236/ijaa.2012.24033](https://doi.org/10.4236/ijaa.2012.24033)
- Ding, G. Q., Qu, J. L., & Li, T. P. 2006a, *The Astronomical Journal*, 131, 1693, doi: [10.1086/499921](https://doi.org/10.1086/499921)
- Ding, G. Q., Zhang, S. N., Li, T. P., & Qu, J. L. 2006b, *The Astrophysical Journal*, 645, 576, doi: [10.1086/504308](https://doi.org/10.1086/504308)
- Frank, J., King, A., & Raine, D. 2002, *Accretion Power in Astrophysics*, 2nd edn. (Cambridge University Press), xi–xii, doi: [10.1017/CBO9781139164245](https://doi.org/10.1017/CBO9781139164245)
- Gendreau, K. C., Arzoumanian, Z., & Okajima, T. 2012, in *Proceedings of SPIE*, ed. T. Takahashi, S. S. Murray, & J.-W. A. den Herder, 844313, doi: [10.1117/12.926396](https://doi.org/10.1117/12.926396)
- Gendreau, K. C., Arzoumanian, Z., Adkins, P. W., et al. 2016, in *Proceedings of SPIE*, ed. J.-W. A. den Herder, T. Takahashi, & M. Bautz, 99051H, doi: [10.1117/12.2231304](https://doi.org/10.1117/12.2231304)
- Groot, P. J., Rutten, R. G. M., & van Paradijjs, J. 2001, *Astronomy and Astrophysics*, 368, 183
- Heinz, S., Sell, P., Fender, R. P., et al. 2013, *The Astrophysical Journal*, 779, 171, doi: [10.1088/0004-637X/779/2/171](https://doi.org/10.1088/0004-637X/779/2/171)
- Heinz, S., Burton, M., Braiding, C., et al. 2015, *The Astrophysical Journal*, 806, 265, doi: [10.1088/0004-637X/806/2/265](https://doi.org/10.1088/0004-637X/806/2/265)
- Hellier, C. 1996, *Astrophysical Journal*, 471, 949, doi: [10.1086/178021](https://doi.org/10.1086/178021)
- Hynes, R. I., Charles, P. A., Haswell, C. A., Casares, J., & Zurita, C. 2001, *Astrotomography. Lecture Notes in Physics*, 573, doi: https://doi.org/10.1007/3-540-45339-3_26
- Iaria, R., Burderi, L., Di Salvo, T., La Barbera, A., & Robba, N. R. 2001, *The Astrophysical Journal*, 547, 412, doi: [10.1086/318366](https://doi.org/10.1086/318366)
- Iaria, R., Di Salvo, T., Robba, N. R., & Burderi, L. 2002, *The Astrophysical Journal*, 567, 503, doi: [10.1086/338507](https://doi.org/10.1086/338507)
- Iaria, R., Spano, M., Di Salvo, T., et al. 2005, *The Astrophysical Journal*, 619, 503, doi: [10.1086/426422](https://doi.org/10.1086/426422)
- Jimenez-Garate, M. A., Raymond, J. C., & Liedahl, D. A. 2002, *The Astrophysical Journal*, 581, 1297, doi: [10.1086/344364](https://doi.org/10.1086/344364)
- Johnston, H. M., Wu, K., Fender, R., & Cullen, J. G. 2001, *Monthly Notices of the Royal Astronomical Society*, 328, 1193, doi: [10.1046/j.1365-8711.2001.04963.x](https://doi.org/10.1046/j.1365-8711.2001.04963.x)
- Jonker, P. G., Nelemans, G., & Bassa, C. G. 2007, *Monthly Notices of the Royal Astronomical Society*, 374, 999, doi: [10.1111/j.1365-2966.2006.11210.x](https://doi.org/10.1111/j.1365-2966.2006.11210.x)
- Kallman, T., & Bautista, M. 2001, *The Astrophysical Journal Supplement Series*, 133, 221, doi: [10.1086/319184](https://doi.org/10.1086/319184)
- Kallman, T. R., Palmeri, P., Bautista, M. A., Mendoza, C., & Krolik, J. H. 2004, *The Astrophysical Journal Supplement Series*, 155, 675, doi: [10.1086/424039](https://doi.org/10.1086/424039)
- Kaluzienski, L. J., Holt, S. S., Boldt, E. A., & Serlemitsos, P. J. 1976, *The Astrophysical Journal*, 208, 71
- Kinkhabwala, A., Sako, M., Behar, E., et al. 2002, *The Astrophysical Journal*, 575, 732, doi: [10.1086/341482](https://doi.org/10.1086/341482)

- Linares, M., Watts, A., Altamirano, D., et al. 2010, *The Astrophysical Journal*, 719, L84, doi: [10.1088/2041-8205/719/1/L84](https://doi.org/10.1088/2041-8205/719/1/L84)
- Makishima, K., Maejima, Y., Mitsuda, K., et al. 1986, *The Astrophysical Journal*, 308, 635, doi: [10.1086/164534](https://doi.org/10.1086/164534)
- Margon, B., Lampton, M., Bowyer, S., & Cruddace, R. 1971, *The Astrophysical Journal*, 169, L23, doi: [10.1086/180806](https://doi.org/10.1086/180806)
- Matsuoka, M., Kawasaki, K., Ueno, S., et al. 2009, *Publications of the Astronomical Society of Japan*, 61, 999, doi: [10.1093/pasj/61.5.999](https://doi.org/10.1093/pasj/61.5.999)
- Mitsuda, K., Inoue, H., Koyama, K., et al. 1984, *Publications of the Astronomical Society of Japan*, 36, 741
- Nasa High Energy Astrophysics Science Archive Research Center (Heasarc). 2014, HEASoft: Unified Release of FTOOLS and XANADU. <https://ui.adsabs.harvard.edu/abs/2014ascl.soft08004N>
- Nicolson, G. D. 2007, *The Astronomer's Telegram*, 985, 1
- Okajima, T., Soong, Y., Balsamo, E. R., et al. 2016, in *Proceedings of SPIE*, ed. J.-W. A. den Herder, T. Takahashi, & M. Bautz, 99054X, doi: [10.1117/12.2234436](https://doi.org/10.1117/12.2234436)
- Parkinson, P. M. S., Tournear, D. M., Bloom, E. D., et al. 2003, *The Astrophysical Journal*, 595, 333, doi: [10.1086/377193](https://doi.org/10.1086/377193)
- Prigozhin, G., Gendreau, K., Foster, R., et al. 2012, in *Proceedings of SPIE*, ed. A. D. Holland & J. W. Beletic, 845318, doi: [10.1117/12.926667](https://doi.org/10.1117/12.926667)
- Scargle, J. D., Norris, J. P., Jackson, B., Chiang, J., & Hansen, W. W. 2013, *The Astrophysical Journal*, 764, 167, doi: [10.1088/0004-637X/764/2/167](https://doi.org/10.1088/0004-637X/764/2/167)
- Schulz, N. S., & Brandt, W. N. 2002, *The Astrophysical Journal*, 572, 971, doi: [10.1086/340369](https://doi.org/10.1086/340369)
- Schulz, N. S., Kallman, T. E., Galloway, D. K., & Brandt, W. N. 2008, *The Astrophysical Journal*, 672, 1091, doi: [10.1086/523809](https://doi.org/10.1086/523809)
- Schulz, N. S., Kallman, T. E., Heinz, S., et al. 2020, *The Astrophysical Journal*, 891, 150, doi: [10.3847/1538-4357/ab6dc8](https://doi.org/10.3847/1538-4357/ab6dc8)
- Shirey, R. E., Bradt, H. V., Levine, A. M., & Morgan, E. H. 1996, *The Astrophysical Journal*, 469, L21, doi: [10.1086/310264](https://doi.org/10.1086/310264)
- Shirey, R. E., Levine, A. M., & Bradt, H. V. 1999, *The Astrophysical Journal*, 524, 1048, doi: [10.1086/307849](https://doi.org/10.1086/307849)
- Tennant, A. F. 1987, *Monthly Notices of the Royal Astronomical Society*, 226, 971, doi: [10.1093/mnras/226.4.971](https://doi.org/10.1093/mnras/226.4.971)
- Tennant, A. F., Fabian, A. C., & Shafer, R. A. 1986, *Monthly Notices of the Royal Astronomical Society*, 221, 27P, doi: [10.1093/mnras/221s.1.27P](https://doi.org/10.1093/mnras/221s.1.27P)
- van der Klis, M. 2006, in *Compact stellar X-ray sources*. Edited by Walter Lewin & Michiel van der Klis. Cambridge Astrophysics Series, No. 39. Cambridge, UK: Cambridge University Press, 39 – 112, doi: [10.2277/0521826594](https://doi.org/10.2277/0521826594)
- Verner, D. A., Ferland, G. J., Korista, K. T., & Yakovlev, D. G. 1996, *The Astrophysical Journal*, 465, 487, doi: [10.1086/177435](https://doi.org/10.1086/177435)
- White, N. E., & Swank, J. H. 1982, *The Astrophysical Journal*, 253, L61, doi: [10.1086/183737](https://doi.org/10.1086/183737)
- Wilms, J., Allen, A., & McCray, R. 2000, *The Astrophysical Journal*, 542, 914, doi: [10.1086/317016](https://doi.org/10.1086/317016)